Top and bottom surfaces limit carrier lifetime in lead iodide perovskite films

Ye Yang[1][†], Mengjin Yang[1][†], David T. Moore[1], Yong Yan[1,2], Elisa M. Miller[1], Kai Zhu[1]★ and Matthew C. Beard[1]★

Carrier recombination at defects is detrimental to the performance of solar energy conversion systems, including solar cells and photoelectrochemical devices. Point defects are localized within the bulk crystal while extended defects occur at surfaces and grain boundaries. If not properly managed, surfaces can be a large source of carrier recombination. Separating surface carrier dynamics from bulk and/or grain-boundary recombination in thin films is challenging. Here, we employ transient reflection spectroscopy to measure the surface carrier dynamics in methylammonium lead iodide perovskite polycrystalline films. We find that surface recombination limits the total carrier lifetime in perovskite polycrystalline thin films, meaning that recombination inside grains and/or at grain boundaries is less important than top and bottom surface recombination. The surface recombination velocity in polycrystalline films is nearly an order of magnitude smaller than that in single crystals, possibly due to unintended surface passivation of the films during synthesis.

Since 2009 polycrystalline lead halide perovskite thin films have become a phenomenon in photovoltaic research[1], and now perovskite-based solar cells routinely exceed 20% power conversion efficiency[2–4]. The extraordinary photovoltaic performance is attributed to beneficial physical properties such as strong light absorption, long carrier lifetime[5,6] and a large carrier diffusion coefficient[5,7–9]. These already remarkable properties are generally improved in single-crystal samples[10–13]. In addition, surface recombination is an essential property that directly impacts the photovoltaic performance. Any surface recombination can reduce the overall carrier lifetime[14–17] and thereby reduce the conversion efficiency[4]. Furthermore, surface recombination plays an important role in other perovskite-based optoelectronic applications. For instance, fast surface recombination can be employed to design photodetectors[18–20], while low surface recombination is required for lasers[21,22] and light-emitting diodes[23]. Thus, the study of surface recombination is key for improving and expanding perovskite-based optoelectronic applications. However, in contrast to the thorough investigation of bulk recombination[24–28], surface recombination in lead iodide perovskites has not been examined.

Here, we study surface recombination in both polycrystalline and single-crystal methylammonium lead iodide perovskite samples by using transient reflection (TR) spectroscopy. As the TR kinetics directly probe the surface carrier dynamics[29], values for the diffusion coefficient and surface recombination velocity (SRV) can be extracted by modelling the data using diffusion equations that include surface recombination. We find that the SRV in the polycrystalline films is nearly an order of magnitude smaller than that found in the single-crystal sample and is comparable to that of passivated conventional semiconductors that are employed for high-efficiency photovoltaics. Our result suggests that surface recombination in polycrystalline films is suppressed by unintended surface passivation that is absent in single crystals, which appears

to be related to an excess of methylammonium compared with the single crystals' surfaces, determined by X-ray photoelectron spectroscopy analysis. Our findings also highlight that despite the low SRV the total carrier lifetime in polycrystalline thin films is still limited by surface recombination rather than recombination inside grains and/or at grain boundaries, suggesting that intentional surface passivation or interface engineering is a key parameter to further improve perovskite solar cell performance.

Sample characterization

The single-crystal samples are grown using an acid-initiated, high-temperature crystallization (see Methods) and show well-defined surfaces[30]. The best fit to the single-crystal diffraction yields low R values and few errant reflections confirming the quality of the single crystal (Supplementary Fig. 1). The polycrystalline perovskite films were prepared using a non-stoichiometric precursor with excess methylammonium iodide[31]. The polycrystalline samples with grain sizes over 1 µm (Supplementary Fig. 2) are in the tetragonal crystal phase (Supplementary Fig. 3). Solar cells fabricated on the basis of these polycrystalline films exhibit a power conversion efficiency of >18% with stable power conversion efficiency output of 17.8% (Supplementary Fig. 4), indicating the high quality of the films. The complex refractive indices as a function of photon energy $(\hbar\omega), \tilde{n}(\hbar\omega) = n(\hbar\omega) + ik(\hbar\omega)$, for both samples are measured by ellipsometry (Supplementary Fig. 5). We can estimate that our TR measurement is sensitive only to carriers that reside within 20 nm of the surface according to the refractive indices. Both samples show a similar absorption coefficient $\alpha(\hbar\omega)$, determined from the corresponding $k(\hbar\omega)$. The absorption coefficient (Fig. 1) exhibits two spectral features at 1.64 and 2.55 eV. The absorption onset can be decomposed, using Elliott's model (inset for single crystal)[29,32,33], into an exciton transition and continuum transitions. The exciton binding energy is found to be 9.5 ± 0.3 meV, consistent with

[1]Chemistry and Nanoscience Center, National Renewable Energy Laboratory, Golden, Colorado 80401, USA. [2]Department of Chemistry and Environmental Science, New Jersey Institute of Technology, Newark, New Jersey 07102, USA. [†]These authors contributed equally to this work. *e-mail: kai.zhu@nrel.gov; matt.beard@nrel.gov
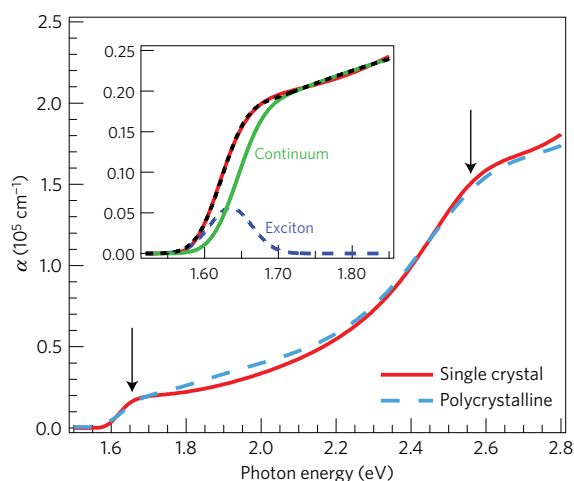
1

Figure 1 | Absorption coefficient $\alpha(\hbar\omega)$ spectra. Both the single-crystal (red trace) and polycrystalline (cyan dashed trace) samples exhibit two spectral features denoted by black arrows. Inset: The band-edge absorption of the single crystal (red trace) is simulated by Elliott's model (black dashed trace), which can be deconvolved into a contribution from exciton absorption (blue dashed trace) and continuum absorption (green trace).

previous reports[28,32,34]. The absorption feature at 2.55 eV has been attributed to both a band edge transition at the M point[35] and a transition from a lower valence band to the conduction band minimum at the R point in the Brillouin zone[8,26].

Transient reflection spectroscopic measurements

Both single- and polycrystalline samples are measured by pump–probe TR spectroscopy. The pump pulse is monochromatic, while the probe pulse consists of a broadband white-light continuum with photon energies in the range of 2.75–1.52 eV. Pseudocolour images (Fig. 2a,b) are employed to show the TR spectra of the samples at different pump–probe delays. Prototypical TR spectra, captured at 5 ps delay, are shown in Fig. 2c,d (red traces) for the single-crystal and polycrystalline samples, respectively. We first consider the TR spectra (Fig. 2a,c) of the single-crystal sample where two features are resolved, a pair of anti-symmetric peaks centred at 1.64 eV and a negative feature at 2.55 eV. The magnitudes of the spectral features decay as the delay increases, yet the spectral shapes persist. As n is more than 20 times larger than k at the band edge (Supplementary Fig. 5), the TR spectrum is approximately proportional to the change in refractive index, $\Delta n(\hbar\omega)$[29,36]. According to the Kramers–Kronig relationship, the inverse Hilbert transform (iHT) of $\Delta n(\hbar\omega)$ is proportional to $\Delta\alpha(\hbar\omega)$, and thus iHT of the TR spectrum can represent the transient absorption (TA) spectrum (see Supplementary Note 1 for details). Figure 2c shows that the anti-symmetric peaks in the TR spectrum correspond to a negative symmetric peak centred at 1.64 eV in the iHT. Similar $\Delta\alpha(\hbar\omega)$ spectra have been reported for perovskite films when measured using TA and are attributed to bleaching of the exciton transition under low excitation fluences[28,32]. Therefore, the anti-symmetric bands in the TR spectra arise due to the bleach of the exciton transition. Because of the small exciton binding energy (9.5 ± 0.3 meV), free carriers will not form excitons after photoexcitation. Rather, the exciton bleach is caused by phase-space filling in the presence of free photocarriers[28,32]. Bleaching of the continuum due to band filling does not contribute to the observed $\Delta\alpha(\hbar\omega)$ because it coincidently cancels with the lower energy part of a photo-induced absorption resulting from bandgap renormalization[32]. The negative peak at 2.55 eV coincides with the second absorption feature in the linear absorption spectrum and corresponds to a bleach of the high-energy absorption

feature that has been observed in TA studies for lead iodide perovskite films[8,26].

The TR spectra of the polycrystalline sample (Fig. 2b,d) are more complicated. In contrast to the single-crystal case, the probe light reflected from both the front and back surface of the thin film can construct interference fringes in the reflectance spectrum. A set of sharp oscillations observed in the TR spectra (Fig. 2b) between probe-photon energies of 1.5 to 1.7 eV can be attributed to the photomodulation of an inference fringe pattern due to changes in $\tilde{n}$ following optical excitation[37,38]. The oscillations occur only near the band edge as higher energy photons are significantly attenuated by absorption. To separate the component of the TR spectrum that arises solely from the front surface, we performed a Hilbert transform (HT) of a TA spectrum (dashed blue trace, Fig. 2d) for the same sample and compared it with the total TR spectrum. The complete TA data are shown in Supplementary Fig. 6. The Kramers–Kronig relationship relates the HT of a TA spectrum within the probing region to its TR spectrum. In accordance, we find that a linearly scaled HT (dashed blue trace) matches the TR (red trace) from 1.7 to 2.0 eV, indicating that in this spectral region the TR spectrum arises from bleaching of the exciton transition. Therefore, the TR spectrum in the overlapping region (from 1.7 to 2.0 eV) is caused exclusively by the change in reflectance at the front surface. Furthermore, we overlay the optical penetration depth ($1/\alpha$) as a function of photon energy (dashed cyan trace, Fig. 2d). For probe photons with energy greater than 1.7 eV, the optical penetration depth (<0.5 μm) is much shorter than twice the film thickness (2 × 0.95 μm), further supporting our assignment that the recorded TR response above 1.7 eV arises only from the front surface reflection. The HT of the TA spectrum for the polycrystalline sample is consistent with the TR spectrum for single crystals (Supplementary Fig. 6), suggesting that the primary discrepancy of the measured TR spectra between the two samples (Fig. 2c,d) is due to the additional photo-induced interference in the polycrystalline sample. The photo-induced interference is then deconvolved from the spectrum by subtracting the scaled HT of the TA from the total TR. Similar to the single crystal, the high-energy TR band corresponding to the second absorption feature is also observed.

The kinetics of the anti-symmetric peaks for both polycrystalline and single-crystal samples are displayed in Fig. 3 (red and blue traces, respectively). As discussed in the previous sections, the anti-symmetric bands in TR spectra for both samples arise from the exciton bleach. According to the phase-space filling theory, the exciton bleach linearly depends on the free carrier density, and thus the TR kinetics in Fig. 3 represent the dynamics of carriers in the probing depth (∼20 nm)[29], referred to as surface carrier dynamics. Also plotted are the TA kinetics of the exciton bleach (black trace, Fig. 3) and the kinetics of interference (green trace, Fig. 3) isolated from the total TR spectra for the polycrystalline film. The TA and interference measurement require the probe to transmit through the film once for the TA measurement or twice for the interference signal. Therefore, the total carrier dynamics can be represented by these independently measured spectral kinetics. In accordance, the similarity of these two kinetic traces implies that they probe the same dynamic process. The slow decay of TA and interference kinetics indicates a long total carrier lifetime in the polycrystalline films. Using nanosecond TA spectroscopy, the total carrier lifetime is measured as 90.0 ± 2.2 ns (Supplementary Fig. 7). The total carrier lifetime in the films depends on both bulk recombination and surface recombination; the quantitative relationship will be discussed later. The bulk carrier lifetime in the single-crystal samples is determined to be 1.6 μs by two-photon excitation time-resolved photoluminescence (Supplementary Fig. 7).

In contrast to the long total carrier lifetimes, the fast decay of the TR kinetics in both samples indicates a short surface carrier lifetime. There are two main causes of the fast surface carrier
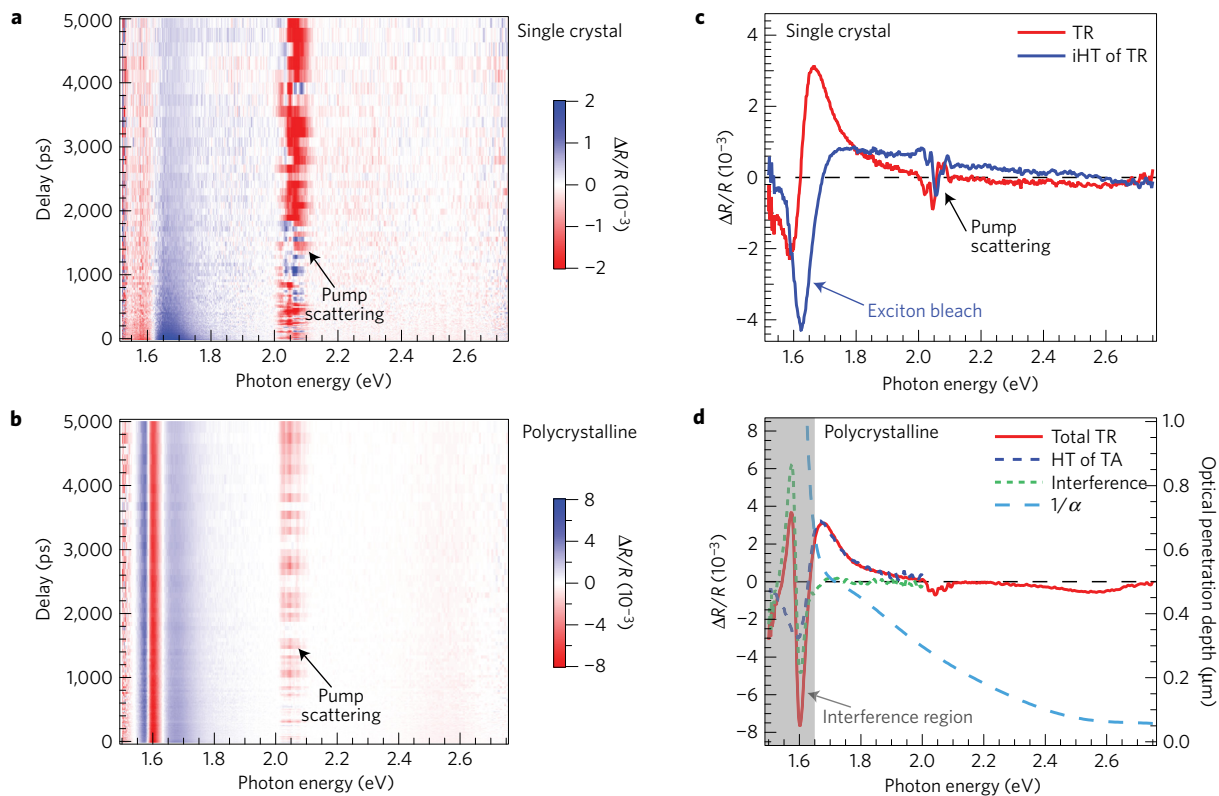
Figure 2 | Transient reflection measurements. The pump-photon energy is 2.07 eV. **a,b**, Pseudocolour images of TR spectra for single-crystal (**a**) and polycrystalline (**b**) samples. The horizontal and vertical axes are the probe-photon energy and pump–probe delay, respectively. The colour intensity indicated by the colour scale bar represents the TR signal magnitude. Blue and red colours indicate an increase or decrease in the reflectance after photoexcitation, respectively. The pump scattering leads to the noise (black arrow) at 2.07 eV. **c,d**, The TR spectra captured at 5 ps delay (red traces) for single-crystal (**c**) and polycrystalline (**d**) samples are also displayed. The inverse Hilbert transform (iHT) of the TR spectrum (blue trace) shown in **c** represents the surface transient absorption spectrum through the Kramers–Kronig relationship. Also shown in **d** are the Hilbert transform of the TA spectrum (blue trace) and photo-induced interference (green trace) deconvolved from the total TR. The dashed cyan trace is the optical penetration depth as a function of photon energy and corresponds to the right axis. The spectral features in the grey shaded region result from the interference in the thin film.

depopulation. First, carrier diffusion takes carriers away from the surface, reducing the surface carrier density. Carriers that are created by light absorption have an initial concentration gradient. The initial carrier distribution is governed by the absorption coefficient at the pump-photon energy and the carrier density drops exponentially from the surface towards the bulk. Diffusion reduces a carrier density gradient, resulting in a decrease of the surface carrier density. Second, surface recombination also impacts the surface carrier lifetime. Surface defects can introduce carrier traps that will reduce the surface carrier lifetime. Therefore, the fast surface carrier depopulation originates from both diffusion and surface recombination[29,39]. Furthermore, the kinetic comparison shows that, pumped at the same photon energy, the surface carriers in the single crystal decay faster than for the polycrystalline sample (compare the blue and red traces in Fig. 3). This difference implies a larger diffusion coefficient and/or a larger surface recombination in the single crystal than in the polycrystalline sample.

Determination of surface recombination velocity
To quantify the diffusion and surface recombination in both samples, additional TR measurements are conducted by varying the pump-photon energy. The photocarrier densities are controlled to be less than 5×10^{17} cm^{-3} (Supplementary Tables 2 and 3), and bulk carrier recombination is negligible for time delays shorter than 5 ns (See Supplementary Note 2 for additional discussion). The normalized pump-energy-dependent kinetics for single-crystal and polycrystalline samples are shown in Fig. 4a,b, respectively. The absorption coefficient monotonically increases as the photon energy

increases (Fig. 1). Therefore, according to the Beer–Lambert law, a pump with higher photon energy always leads to a larger gradient of the initial photocarrier density and thus a faster surface decay dynamics due to a larger diffusion rate. To quantitatively describe the carrier density evolution under the various optical excitation conditions, a one-dimensional diffusion equation is employed,

$$\frac{\partial N(x,t)}{\partial t} = D \frac{\partial^2 N(x,t)}{\partial x^2} - \frac{N(x,t)}{\tau_B} \tag{1}$$

where $N(x, t)$ is the carrier density as a function of depth (x) and time (t), D is the ambipolar diffusion coefficient and τ_B is the bulk carrier lifetime. In comparison with the timescale for carrier diffusion, the pulsed carrier generation is assumed to be instantaneous, and the initial condition for equation (1) is then given by

$$N(x,0) = N_0 \cdot \exp(-\alpha x) \tag{2}$$

where N_0 is the initial surface carrier density, such that $N_0 = \alpha(1 - R)J_0$, where J_0 is the pump fluence and R is the reflectance at the pump-photon energy. If the traces are normalized, then N_0 is equal to 1. The values for the absorption coefficient α at different pump-photon energies for both samples are known (taken from Fig. 1).

For the single crystal, the boundary conditions are described as

$$\left.\frac{\partial N(x,t)}{\partial t}\right|_{x=0} = \frac{S}{D} N(0,t) \tag{3}$$
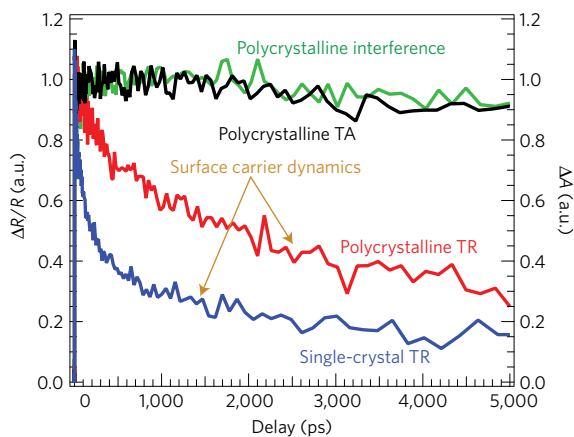
Figure 3 | Surface and total carrier dynamics. The surface carrier dynamics extracted from the TR spectra for the single-crystal (blue trace) and polycrystalline samples (red trace). The total carrier dynamics in the polycrystalline sample is independently measured by the TA kinetics (black trace) and the interference dynamics (green trace) that is isolated from the total TR spectra. The TA kinetics (black trace) corresponds to the right axis. The kinetics for the single crystal is recorded at 1.7 eV, while it is recorded at 1.75 eV for the polycrystalline sample to completely avoid the influence of the interference. For a convenient comparison, all kinetic traces are normalized to their maxima.

and

$$N(L_{SC}, t) = 0 \qquad (4)$$

where L_{SC} is the thickness of the single crystal (4 mm) that is orders of magnitude thicker than the optical penetration depth plus carrier diffusion length, and S is the SRV. Assuming L_{SC} is infinitely long, equation (1) with initial and boundary conditions for the single crystal can be solved analytically, giving an analytical expression of $N(x, t)$ (Supplementary Equation 1 in Supplementary Fig. 7)[29,40]. The measured surface carrier dynamics are described by $N(0, t)$ because the carrier density is nearly constant over the reflected probe detection depth (Supplementary Figs 8 and 9). Thus, the different surface carrier kinetics (Fig. 4a) in the single crystal are simultaneously modelled by $N(0, t)$ using a nonlinear least-squares global fitting routine in which S and D are set as global fitting parameters. The best-fit curves (black traces, Fig. 4a) closely follow the surface kinetic data and resulting parameters are tabulated in Table 1.

For polycrystalline samples the film thickness is no longer larger than the optical penetration depth plus carrier diffusion length and in this case the boundary conditions are described as

$$\left.\frac{\partial N(x, t)}{\partial x}\right|_{x=0} = \frac{S_F}{D} N(0, t) \qquad (5)$$

and

$$\left.\frac{\partial N(x, t)}{\partial x}\right|_{x=L_{PC}} = -\frac{S_B}{D} N(L_{PC}, t) \qquad (6)$$

where L_{PC} is the thickness of the polycrystalline thin film (0.95 μm), and S_F and S_B are the SRVs for the front and back surfaces, respectively. In this case, the diffusion equation cannot be solved analytically; therefore, we solve it numerically by using a backward finite difference method. The kinetic traces in Fig. 4b are simultaneously modelled using the numerical solution, $N(0, t)$ in a global fitting routine. The comparison of the TR kinetics collected from the front and back surface (Supplementary Fig. 10) indicates that S_F is similar to S_B. To reduce the number of fitting
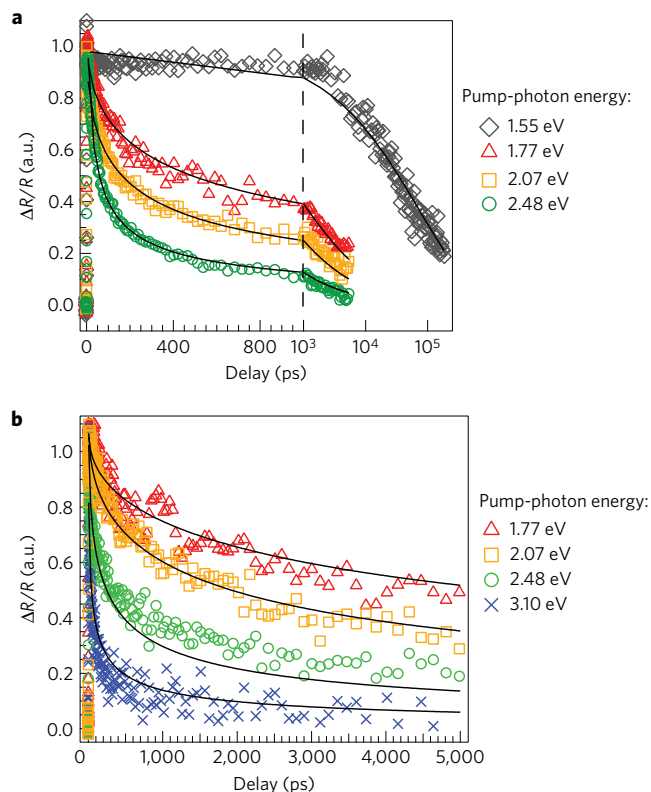

Figure 4 | Surface kinetics with different pump-photon energies. a,b, The normalized surface carrier kinetics of single-crystal (**a**) and polycrystalline (**b**) samples photoexcited at the indicated photon energies. The black solid traces are nonlinear least-squares global best-fit curves for the single-crystal and polycrystalline sample, respectively (details found in the text). The x axis of **a** is split into two parts to clearly show the kinetics and fits. The first part (−5 to 1,000 ps) and second part (1–200 ns) are plotted on linear and logarithmic scales, respectively.

parameters, we make S_F and D vary freely as global variables, and S_B is set the same as S_F during the fitting process. As indicated in Fig. 3, the bulk carrier recombination in the polycrystalline film is negligible in a 5 ns delay window, and thus the contribution of bulk recombination in equation (1) is neglected. The best-fit curves (black traces) successfully reproduce the TR kinetics (Fig. 4b), and the parameters are listed in Table 1.

Discussion

We find that D for the single crystal is about 11 times larger than that for the polycrystalline thin films (Table 1). For the single crystal, D measured here is consistent with reported values measured by time-resolved photoluminescence[41], time-of-flight[11] and space-charge-limited current techniques[12,42], but an order of magnitude smaller than that determined from terahertz spectroscopy[13]. For the polycrystalline films, the measured D value also falls in the reported range (from 0.01 to 0.3 cm² s⁻¹) obtained from different methods[5–8,43–45]. The SRV for the single-crystal samples is in good agreement with the reported values for untreated surfaces of methylammonium lead bromide perovskite single crystals[18,29]. Usually, single-crystal samples have a lower bulk defect density than polycrystalline films, accounting for the larger diffusion coefficient and longer total carrier lifetimes[11,12]. Surprisingly, the SRV in the polycrystalline samples is more than six times lower than that in the single crystals, suggesting significantly less surface defects in the polycrystalline films. Therefore, the polycrystalline surfaces must be protected from defects, and this unintended passivation possibly arises during the synthetic processes.

Table 1 | List of best-fit parameters.

	D (cm^2 s^{-1})	S (10^3 cm s^{-1})
Single crystal	1.9 ± 0.1	2.8 ± 0.1
Polycrystalline	0.17 ± 0.01	0.45 ± 0.14

The ambipolar diffusion coefficient (D) and SRV (S) are set as free fitting parameters. For the polycrystalline sample, the SRVs for the front and back surfaces are assumed to be the same in the fitting. The errors represent only the uncertainty of the fitting.

To explore the differences in the surface passivation, the surface chemical stoichiometry of both samples is examined by X-ray photoelectron spectroscopy (XPS; Supplementary Fig. 11). The elemental analysis indicates that the single-crystal surface is Pb^{2+}-rich, while the polycrystalline surface is C- and N-rich (Supplementary Table 1), which we believe results from methylammonium (MA$^+$) surface termination. Combining the XPS and TR results for both samples, we find that the suppressed surface recombination for the polycrystalline sample is possibly due to the MA-rich chemistry environment. We also examine the stoichiometry (Supplementary Table 1) and surface recombination dynamics (Supplementary Fig. 12) on a polished surface of the single-crystal sample, and we find a similar element ratio and SRV to those for the original surface of the single crystal. The observation of suppressed surface recombination at MA$^+$-rich surfaces is consistent with a previous report concluding that a methylammonium iodide layer can passivate perovskite grain boundaries[46]. Although the physical environment of the film surfaces is different from the grain boundaries, this consistency suggests they may share similar principles for chemical passivation. Incidentally, some reports find excess MAI[31], while others find PbI$_2$ (refs 16,46,47), can lead to significantly improved device performance, presumably due to increased carrier lifetime through grain-boundary passivation. However, in those reports, the non-stoichiometric reactant may lead to the change of grain size of the films[48], which can also cause the total carrier lifetime enhancement[29,48]. In addition, the chemical nature of the grain boundaries is not determined and cannot be directly correlated to the carrier lifetime increase. Therefore, in those studies the mechanism for boundary passivation remains unclear. The SRV in the polycrystalline films is 3–4 orders of magnitude lower than that in unpassivated photovoltaic semiconductors ($S = 10^5$–10^6 cm s^{-1}) (ref. 29) and comparable to the SRV in semiconductors after sophisticated passivation ($S = 10$–10^2 cm s^{-1}) for high-efficiency photovoltaics[49–51].

In the polycrystalline thin films, the total carrier lifetime (τ_T) depends on both the bulk lifetime and SRV, and the relationship is given by[52]

$$\frac{1}{\tau_T} = \frac{1}{\tau_B} + \frac{1}{\frac{L_{PC}}{2S} + \frac{1}{D}\left(\frac{L_{PC}}{\pi}\right)^2} \qquad (7)$$

where τ_B is the bulk carrier lifetime. τ_T is determined as 90.0 ± 2.2 ns (Supplementary Fig. 7). Substituting all the known values in equation (7), for the polycrystalline film, τ_B is determined to be 477 ± 61 ns. It should be noted that, under low excitation intensity, τ_B for lead iodide perovskites is primarily determined by the first-order recombination (Shockley–Read–Hall recombination) due to defects at grain boundaries and inside grains. The above estimation suggests that, despite the already low SRV, the total lifetime of the polycrystalline film is still limited by top and bottom surface recombination. It is worth noting that for the polycrystalline perovskites used in high-efficiency solar cells the reported total carrier lifetimes are on the timescale of 100 ns (refs 7,46,53), similar to the value found here. According to our results the total lifetime could be increased by a factor of 5 following complete surface passivation. To increase the total lifetime into the microsecond

regime (limited by radiative recombination), defect density for both bulk (including grain boundaries) and surfaces needs to be decreased.

Solar energy conversion requires the photo-induced production of long-lived charge carriers that can be separated to generate a photovoltage and photocurrent. Understanding and reducing all charge carrier loss channels is essential for achieving the ultimate thermodynamically limited conversion efficiency. Here, using TR spectroscopy, we separate the surface carrier dynamics from bulk carrier dynamics in single-crystal and polycrystalline methylammonium lead iodide perovskites. We find that the total carrier lifetime in polycrystalline films is limited by recombination at top and bottom surfaces. Surprisingly, our results indicate that the SRV in the polycrystalline films is nearly an order of magnitude smaller than that in single crystals, which is possibly due to an unintended surface passivation in polycrystalline films. Clearly, the development of single-crystal perovskite optoelectronics can be accelerated if effective surface passivation is achieved. Surface chemical analysis indicates that the polycrystalline films are MA-rich relative to the single crystals. Our results suggests that further investigation into surface passivation is needed to effectively increase the total carrier lifetime and thereby improve the performance of optoelectronic applications such as solar cells, light-emitting diodes and lasers.

Methods

Transient reflectance spectroscopy. The TR measurements were performed by a pump–probe spectrometer. The fundamental laser pulse with wavelength at 800 nm is generated by a Ti:sapphire amplifier. The pulse repetition rate is 1 kHz. The fundamental pulse is then split into two parts by a beam splitter. One part is sent to an optical parametric amplifier for the pump generation. The pump is chopped at a frequency of 500 Hz and attenuated by neutral density filter wheels. The other part of the fundamental pulse is focused into a sapphire crystal to generate a white-light continuum (430–820 nm) that is used as the probe. The probe pulses are delayed in time with respect to the pump pulses using a motorized translation stage mounted with a retroreflecting mirror. The pump and probe are spatially overlapped on the surface of the sample. The incident angle for both pump and probe is around 45°. The reflected probe pulses are directed to the multichannel complementary metal–oxide–semiconductor sensor. The size of the focused spot at the sample position for the probe and pump beams is around 200 μm and 600 μm, respectively. The total pump-photon flux is determined by measuring the pump power after a pinhole with a radius of 200 μm at the sample position. The input photon flux is obtained by subtracting the reflected photon flux from the total photon flux. The average excitation density is calculated as the ratio of input photon flux to the pump penetration depth. The pump-photon flux and the average excitation density are provided in Supplementary Tables 2 and 3.

Preparation of CH$_3$NH$_3$PbI$_3$ single crystals. Single crystals were prepared using a method similar to that previously reported[30]. Briefly, iodide salt solutions at 0.8 M in 4 ml fresh γ-butyrolactone were prepared by dissolving the salts at 55 °C with vigorous stirring for at least 30 min. Formic acid (280 μl) was then added and the solution was filtered with a 0.45 μm syringe filter and placed in an oil bath at 95 °C in a closed crystallization dish. After the initial seed growth, an appropriate seed crystal (∼0.5 mm) was placed in a similarly prepared solution and allowed to grow for 10–12 h. The process was repeated 4 times yielding a single crystal ∼10 mm × 8 mm at the base and 4 mm thick. After the growth process, the single crystal was immediately coated by a thin poly(methyl methacrylate) (PMMA) layer for the optical measurements.

Preparation of CH$_3$NH$_3$PbI$_3$ polycrystalline films. Non-stoichiometric precursor was prepared by dissolving methylammonium iodide (MAI) and lead iodide (PbI$_2$) (MAI/PbI$_2$ = 1.2:1) in mixed solvents (NMP/GBL =7:3 wt) to form ∼62 wt% solution. Glass substrate, with 100 μl precursor solution, was spun at 3,000 r.p.m. for 25 s, and was transferred into an ether bath for 90 s. Dark black perovskite film was crystallized in the bath, and was further annealed at 150 °C for 15 min with a Petri dish covered to remove excess MAI. A thin PMMA layer (∼30 nm) was coated on top of the perovskite film to protect it from moisture ingress.

X-ray photoelectron spectroscopy (XPS). XPS data were obtained on a Physical Electronics 5600 system using Al Kα radiation. Briefly, the XPS set-up was calibrated with Au metal, which was cleaned via Ar-ion sputtering. The raw

atomic concentration has a 5% error due to surface inhomogeneities, surface roughness, literature sensitivity values for peak integration, and so on. Both single-crystal and polycrystalline samples were measured without PMMA coatings.

References

1. Kojima, A., Teshima, K., Shirai, Y. & Miyasaka, T. Organometal halide perovskites as visible-light sensitizers for photovoltaic cells. *J. Am. Chem. Soc.* **131**, 6050–6051 (2009).
2. Yang, W. S. *et al.* High-performance photovoltaic perovskite layers fabricated through intramolecular exchange. *Science* **348**, 1234–1237 (2015).
3. Saliba, M. *et al.* A molecularly engineered hole-transporting material for efficient perovskite solar cells. *Nat. Energy* **1**, 15017 (2016).
4. Bi, D. *et al.* Efficient luminescent solar cells based on tailored mixed-cation perovskites. *Sci. Adv.* **2**, e1501170 (2016).
5. Wehrenfennig, C., Eperon, G. E., Johnston, M. B., Snaith, H. J. & Herz, L. M. High charge carrier mobilities and lifetimes in organolead trihalide perovskites. *Adv. Mater.* **26**, 1584–1589 (2014).
6. Savenije, T. J. *et al.* Thermally activated exciton dissociation and recombination control the carrier dynamics in organometal halide perovskites. *J. Phys. Chem. Lett.* **5**, 2189–2194 (2014).
7. Stranks, S. D. *et al.* Electron-hole diffusion lengths exceeding 1 micrometer in an organometal trihalide perovskite absorber. *Science* **342**, 341–344 (2013).
8. Xing, G. *et al.* Long-range balanced electron- and hole-transport lengths in organic–inorganic $CH_3NH_3PbI_3$. *Science* **342**, 344–347 (2013).
9. Ponseca, C. S. Jr *et al.* Organometal halide perovskite solar cell materials rationalized: ultrafast charge generation, high and microsecond-long balanced mobilities, and slow recombination. *J. Am. Chem. Soc.* **136**, 5189–5192 (2014).
10. Bi, Y. *et al.* Charge carrier lifetimes exceeding 15 μs in methylammonium lead iodide single crystals. *J. Phys. Chem. Lett.* **7**, 923–928 (2016).
11. Dong, Q. *et al.* Electron-hole diffusion lengths >175 μm in solution-grown $CH_3NH_3PbI_3$ single crystals. *Science* **347**, 967–970 (2015).
12. Shi, D. *et al.* Low trap-state density and long carrier diffusion in organolead trihalide perovskite single crystals. *Science* **347**, 519–522 (2015).
13. Valverde-Chavez, D. A. *et al.* Intrinsic femtosecond charge generation dynamics in single crystal $CH_3NH_3PbI_3$. *Energy Environ. Sci.* **8**, 3700–3707 (2015).
14. Noel, N. K. *et al.* Enhanced photoluminescence and solar cell performance via lewis base passivation of organic–inorganic lead halide perovskites. *ACS Nano* **8**, 9815–9821 (2014).
15. deQuilettes, D. W. *et al.* Impact of microstructure on local carrier lifetime in perovskite solar cells. *Science* **348**, 683–686 (2015).
16. Chen, Q. *et al.* Controllable self-induced passivation of hybrid lead iodide perovskites toward high performance solar cells. *Nano Lett.* **14**, 4158–4163 (2014).
17. Wu, X. *et al.* Trap states in lead iodide perovskites. *J. Am. Chem. Soc.* **137**, 2089–2096 (2015).
18. Wei, H. *et al.* Sensitive X-ray detectors made of methylammonium lead tribromide perovskite single crystals. *Nat. Photon.* **10**, 333–339 (2016).
19. Fang, Y., Dong, Q., Shao, Y., Yuan, Y. & Huang, J. Highly narrowband perovskite single-crystal photodetectors enabled by surface-charge recombination. *Nat. Photon.* **9**, 679–686 (2015).
20. Dou, L. *et al.* Solution-processed hybrid perovskite photodetectors with high detectivity. *Nat. Commun.* **5**, 5404 (2014).
21. Zhu, H. *et al.* Lead halide perovskite nanowire lasers with low lasing thresholds and high quality factors. *Nat. Mater.* **14**, 636–642 (2015).
22. Xing, G. *et al.* Low-temperature solution-processed wavelength-tunable perovskites for lasing. *Nat. Mater.* **13**, 476–480 (2014).
23. Tan, Z.-K. *et al.* Bright light-emitting diodes based on organometal halide perovskite. *Nat. Nanotech.* **9**, 687–692 (2014).
24. Wehrenfennig, C., Liu, M., Snaith, H. J., Johnston, M. B. & Herz, L. M. Charge-carrier dynamics in vapour-deposited films of the organolead halide perovskite $CH_3NH_3PbI_{3−x}Cl_x$. *Energy Environ. Sci.* **7**, 2269–2275 (2014).
25. Rehman, W. *et al.* Charge-carrier dynamics and mobilities in formamidinium lead mixed-halide perovskites. *Adv. Mater.* **27**, 7938–7944 (2015).
26. Manser, J. S. & Kamat, P. V. Band filling with free charge carriers in organometal halide perovskites. *Nat. Photon.* **8**, 737–743 (2014).
27. Price, M. B. *et al.* Hot-carrier cooling and photoinduced refractive index changes in organic–inorganic lead halide perovskites. *Nat. Commun.* **6**, 8420 (2015).
28. Yang, Y. *et al.* Comparison of recombination dynamics in $CH_3NH_3PbBr_3$ and $CH_3NH_3PbI_3$ perovskite films: influence of exciton binding energy. *J. Phys. Chem. Lett.* **6**, 4688–4692 (2015).
29. Yang, Y. *et al.* Low surface recombination velocity in solution-grown $CH_3NH_3PbBr_3$ perovskite single crystal. *Nat. Commun.* **6**, 7961 (2015).
30. Nayak, P. K. *et al.* Mechanism for rapid growth of organic–inorganic halide perovskite crystals. *Nat. Commun.* **7**, 13303 (2016).
31. Yang, M. *et al.* Square-centimeter solution-processed planar $CH_3NH_3PbI_3$ perovskite solar cells with efficiency exceeding 15%. *Adv. Mater.* **27**, 6363–6370 (2015).
32. Yang, Y. *et al.* Observation of a hot-phonon bottleneck in lead-iodide perovskites. *Nat. Photon.* **10**, 53–59 (2016).
33. Saba, M. *et al.* Correlated electron-hole plasma in organometal perovskites. *Nat. Commun.* **5**, 5049 (2014).
34. Miyata, A. *et al.* Direct measurement of the exciton binding energy and effective masses for charge carriers in organic–inorganic tri-halide perovskites. *Nat. Phys.* **11**, 582–587 (2015).
35. Even, J., Pedesseau, L. & Katan, C. Analysis of multivalley and multibandgap absorption and enhancement of free carriers related to exciton screening in hybrid perovskites. *J. Phys. Chem. C* **118**, 11566–11572 (2014).
36. Sorenson, S. A., Patrow, J. G. & Dawlaty, J. M. Electronic dynamics in natural iron pyrite studied by broadband transient reflection spectroscopy. *J. Phys. Chem. C* **120**, 7736–7747 (2016).
37. Joly, A. G. *et al.* Carrier dynamics in α-Fe_2O_3 (0001) thin films and single crystals probed by femtosecond transient absorption and reflectivity. *J. Appl. Phys.* **99**, 053521 (2006).
38. Eid, J. *et al.* Ultrafast pump–probe reflectance spectroscopy: why sodium makes $Cu(In,Ga)Se_2$ solar cells better. *Sol. Energy Mater. Sol. Cells* **140**, 33–37 (2015).
39. Yang, Y. *et al.* Semiconductor interfacial carrier dynamics via photoinduced electric fields. *Science* **350**, 1061–1065 (2015).
40. Beard, M. C., Turner, G. M. & Schmuttenmaer, C. A. Transient photoconductivity in GaAs as measured by time-resolved terahertz spectroscopy. *Phys. Rev. B* **62**, 15764–15777 (2000).
41. Tian, W., Zhao, C., Leng, J., Cui, R. & Jin, S. Visualizing carrier diffusion in individual single-crystal organolead halide perovskite nanowires and nanoplates. *J. Am. Chem. Soc.* **137**, 12458–12461 (2015).
42. Saidaminov, M. I. *et al.* High-quality bulk hybrid perovskite single crystals within minutes by inverse temperature crystallization. *Nat. Commun.* **6**, 8586 (2015).
43. Guo, Z., Manser, J. S., Wan, Y., Kamat, P. V. & Huang, L. Spatial and temporal imaging of long-range charge transport in perovskite thin films by ultrafast microscopy. *Nat. Commun.* **6**, 7471 (2015).
44. Maynard, B. *et al.* Electron and hole drift mobility measurements on methylammonium lead iodide perovskite solar cells. *Appl. Phys. Lett.* **108**, 173505 (2016).
45. Ihly, R. *et al.* Efficient charge extraction and slow recombination in organic–inorganic perovskites capped with semiconducting single-walled carbon nanotubes. *Energy Environ. Sci.* **9**, 1439–1449 (2016).
46. Son, D.-Y. *et al.* Self-formed grain boundary healing layer for highly efficient $CH_3NH_3PbI_3$ perovskite solar cells. *Nat. Energy* **1**, 16081 (2016).
47. Lee, Y. H. *et al.* Unraveling the reasons for efficiency loss in perovskite solar cells. *Adv. Funct. Mater.* **25**, 3925–3933 (2015).
48. Stewart, R. J., Grieco, C., Larsen, A. V., Maier, J. J. & Asbury, J. B. Approaching bulk carrier dynamics in organo-halide perovskite nanocrystalline films by surface passivation. *J. Phys. Chem. Lett.* **7**, 1148–1153 (2016).
49. Royea, W. J., Juang, A. & Lewis, N. S. Preparation of air-stable, low recombination velocity Si(111) surfaces through alkyl termination. *Appl. Phys. Lett.* **77**, 1988–1990 (2000).
50. Cohen, R., Lyahovitskaya, V., Poles, E., Liu, A. & Rosenwaks, Y. Unusually low surface recombination and long bulk lifetime in *n*-CdTe single crystals. *Appl. Phys. Lett.* **73**, 1400–1402 (1998).
51. Zhao, X.-H. *et al.* Determination of CdTe bulk carrier lifetime and interface recombination velocity of CdTe/MgCdTe double heterostructures grown by molecular beam epitaxy. *Appl. Phys. Lett.* **105**, 252101 (2014).
52. Sproul, A. B. Dimensionless solution of the equation describing the effect of surface recombination on carrier decay in semiconductors. *J. Appl. Phys.* **76**, 2851–2854 (1994).
53. You, J. *et al.* Improved air stability of perovskite solar cells via solution-processed metal oxide transport layers. *Nat. Nanotech.* **11**, 75–81 (2016).

Author contributions

Y.Yang carried out the transient reflectance experiment; Y.Yang and M.C.B. analysed the data; E.M.M. carried out the XPS data collection and analysis; M.Y. and K.Z. prepared and characterized the thin-film samples; D.T.M. and Y.Yan prepared the single-crystal samples; Y.Yang and M.C.B. wrote the manuscript with input and discussion from all authors.

Additional information

Supplementary information is available for this paper.

Reprints and permissions information is available at www.nature.com/reprints.

Correspondence and requests for materials should be addressed to K.Z. or M.C.B.

How to cite this article: Yang, Y. *et al.* Top and bottom surfaces limit carrier lifetime in lead iodide perovskite films. *Nat. Energy* **2**, 16207 (2017).

Competing interests

The authors declare no competing financial interests.